From Solidification Processing to Microstructure to Mechanical Properties: A Multi-scale X-ray Study of an Al-Cu Alloy Sample

D. TOURRET, J.C.E. MERTENS, E. LIEBERMAN, S.D. IMHOFF, J.W. GIBBS, K. HENDERSON, K. FEZZAA, A.L. DERIY, T. SUN, R.A. LEBENSOHN, B.M. PATTERSON, and A.J. CLARKE

We follow an Al-12 at. pct Cu alloy sample from the liquid state to mechanical failure, using *in situ* X-ray radiography during directional solidification and tensile testing, as well as three-dimensional computed tomography of the microstructure before and after mechanical testing. The solidification processing stage is simulated with a multi-scale dendritic needle network model, and the micromechanical behavior of the solidified microstructure is simulated using voxelized tomography data and an elasto-viscoplastic fast Fourier transform model. This study demonstrates the feasibility of direct *in situ* monitoring of a metal alloy microstructure from the liquid processing stage up to its mechanical failure, supported by quantitative simulations of microstructure formation and its mechanical behavior.

DOI: 10.1007/s11661-017-4302-8

I. INTRODUCTION

PROGRESS in understanding the links between processing routes, microstructures, properties, and performance of structural technological materials depends on our ability to observe materials *in situ* throughout their life cycle, and to quantitatively simulate these individual links.

In terms of *in situ* imaging, the use of X-ray radiography and computed tomography has spread rapidly within most branches of materials science within the past two decades.[1] These techniques are particularly relevant to metallic alloys, and have been extensively employed in solidification processing,[2–5] three-dimensional (3D) rendering of microstructures and their evolution,[2] and in experimental mechanics.[6] X-ray imaging, in particular 3D tomography, has reached a sufficient level of maturity to be capable of providing quantitative measurements.[7]

Solidification processing of metallic alloys (and in particular aluminum-based alloys) has been thoroughly investigated using two-dimensional (2D) radiography of thin sample experiments, often in controlled directional solidification conditions.[8–22] Resulting studies shed light onto mechanisms such as morphological transitions,[8–11] dendritic and eutectic growth,[11–15] dendritic fragmentation,[16–20] gravity-induced buoyancy and solute transport,[15–17,20,21] and the formation of major solidification defects such as freckles.[21,22]

Metallic alloy solidification and microstructure evolution have also been extensively studied using 3D computed tomography.[23–31] Studies have mostly focused on mechanisms of solidification at low growth rates,[23,24] dendritic coarsening,[25] morphological transitions of equiaxed grains,[31] or the formation of intermetallics.[26,27] Recently, advanced techniques to increase temporal resolution have allowed resolving the evolution of complex dendritic morphologies at higher cooling rates[28,29] and exploring cellular-to-dendritic morphological transitions.[30]

Computed X-ray tomography has also become widespread in the field of experimental mechanics. It has primarily been used to observe mechanical testing of polymers (*e.g.*, Reference 32), metallic alloys (*e.g.*, References 33 through 35), and metallic foams (*e.g.*, References 36 and 37). Recent advances in fast tomography now allow observing the progression of a

D. TOURRET is with the Sigma Division, Los Alamos National Laboratory, P.O. Box 1663, Los Alamos, NM 87545, and also with the IMDEA Materials Institute, Calle Eric Kandel 2, 28906 Getafe, Madrid, Spain. J.C.E. MERTENS, E. LIEBERMAN, K. HENDERSON, R.A. LEBENSOHN, and B.M. PATTERSON are with the Materials Science and Technology Division, Los Alamos National Laboratory, P.O. Box 1663, Los Alamos, NM 87545. S.D. IMHOFF and J.W. GIBBS are with the Sigma Division, Los Alamos National Laboratory. K. FEZZAA, A.L. DERIY, and T. SUN are with the Argonne National Laboratory, Advanced Photon Source, Lemont, IL 60439. A.J. CLARKE is with the Sigma Division, Los Alamos National Laboratory, and also with the Department of Metallurgical and Materials Engineering, Colorado School of Mines, 1500 Illinois Street, Golden, CO 80401. Contact e-mail: amyclarke@mines.edu

Manuscript submitted April 05, 2017.
Article published online September 13, 2017

crack during fracture of materials of increasingly lower ductility (*e.g.*, up to 20 Hz[38]).

At the crossroads of processing and properties, X-ray *in situ* imaging has also been extensively used to investigate the mechanical behavior of semi-solid materials.[39–48] Such studies, usually realized for isothermal conditions with a partially melted sample, have helped to determine key mechanisms of failure or defect formation in a state of tension, *e.g.*, linking the mushy zone permeability and the lack of liquid feeding to hot tearing defects,[40,43,44] as well as in compression,[45–48] highlighting the opening of internal pores[46] or transgranular liquation cracking,[47] for instance.

Other emerging materials characterization methods based on synchrotron X-rays include novel diffraction methods such as 3D X-ray Diffraction Microscopy (3DXRD)[49] or high-energy diffraction microscopy (HEDM).[50] These techniques provide previously inaccessible microstructural information on polycrystalline materials, including *in situ* 3D imaging of local crystal orientation and stresses, enabled by the collection of multiple diffraction patterns obtained by rotating the sample as it is deformed. Near-field HEDM[51,52] allows characterization of crystal orientation fields in the form of voxelized microstructural images, while far-field HEDM[53,54] provides local micromechanical information in the form of average stresses/elastic strains in the single-crystal grains.

In parallel, a host of modeling approaches spanning the wide range of relevant length and time scales have been developed, both in the field of solidification[55–57] and in that of microstructure-informed mechanical behavior, typically using homogenization techniques[58–60] or full-field simulations[61–69] of polycrystalline samples. Most of the experimental studies mentioned in previous paragraphs were combined with numerical simulations, involving methods such as finite elements,[32,33,35–37,41,42] finite volumes,[27] cellular automata,[21,22] granular modeling,[44] or Fast Fourier Transform (FFT)-based methods.[65–69]

Thanks to these advances, our grasp of complex processing-microstructure-properties links in metals has substantially evolved since the pioneering tensile testing experiments of solidifying alloys by Kurz and co-workers in the 1980's.[70] In modern metallurgy, imaging, testing, and simulation are becoming increasingly integrated within each step of the life of a technological part. Modern applications can, for instance, consist of X-ray tomography to determine porosity during selective laser melting processes[71] or punching tests during solidification of a 450 kg steel ingot.[72,73] In this context, the natural evolution for metallurgical research leads toward studies that integrate imaging and modeling of a given material all the way from the liquid state up to the component failure.

While we still have a way to go before reaching fully coupled modeling and process monitoring across all relevant length and time scales, most key pieces are now mature enough to be put together. The current article presents a collaborative effort aimed at following a unique sample from its liquid state up to its failure during tensile testing. First, we directionally solidified an aluminum-copper (Al-12 at. pct Cu) alloy while using synchrotron X-ray radiography. Then, we used microfocus X-ray radiography during tensile testing of the as-solidified thin sample, as well as microfocus tomography before and after tensile testing. Both processing and mechanical testing steps are directly compared to modern simulation techniques, namely a multi-scale dendritic needle network (DNN) model for dendritic solidification,[74,75] and an elasto-viscoplastic micromechanical formulation based on FFTs (EVPFFT model) using a voxelized description of the microstructure.[65] While remaining for the most part exploratory, this work highlights some of the remaining hurdles on the way to achieving through-process monitoring and fully predictive virtual processing and design of structural metallic alloys.

II. MATERIALS AND METHODS

A. *Processing*

1. *Sample preparation*

High purity (99.999 pct) aluminum and copper were arc-melted together to form a button of nominal composition Al-12 at. pct Cu. The button was remelted 10 times in a zirconium-gettered argon atmosphere to achieve homogeneity and was then arc-cast in a copper mold with water cooling, resulting in a disk-like ingot roughly 6 mm thick and 40 mm in diameter. The ingot was electrical discharge machined (EDM), and sliced normal to the thickness direction. The slices were ground flat to remove the EDM re-cast layer to a final thickness of approximately 200 μm. A rectangular section of dimensions 11 mm $\times$ 30 mm was then cut from the foil to be processed in our directional solidification furnace.

2. *Sample solidification*

The thin sample was inserted into a boron nitride crucible consisting of two rectangular plate-like halves with a central smaller rectangular 100 μm deep pocket. The sample foil was placed into the pocket, and the two halves of the crucible were sandwiched together, fully surrounding the foil. The (crucible + sample) assembly was inserted into a steel rod with a central, trans-axial slot the size of the crucible (Figure 1). The steel rod was heated inductively *via* two independently controlled coils around the rod, above and below the crucible. The rod was instrumented with thermocouples to provide temperature monitoring and feedback control.

The sample ends were independently heated to produce a nominal thermal gradient of about 5 K/mm, which was maintained during solidification. The imposed target cooling rate was about 2.0 K/s. The achieved cooling rate was estimated by fitting the temperature evolution of the two thermocouples located on both sides of the observation window (Figure 1(c)). These two thermocouples gave temperature readings within less than one degree of each other, and similar fitted cooling rates up to the third significant figure. The temperature gradient was estimated as the difference

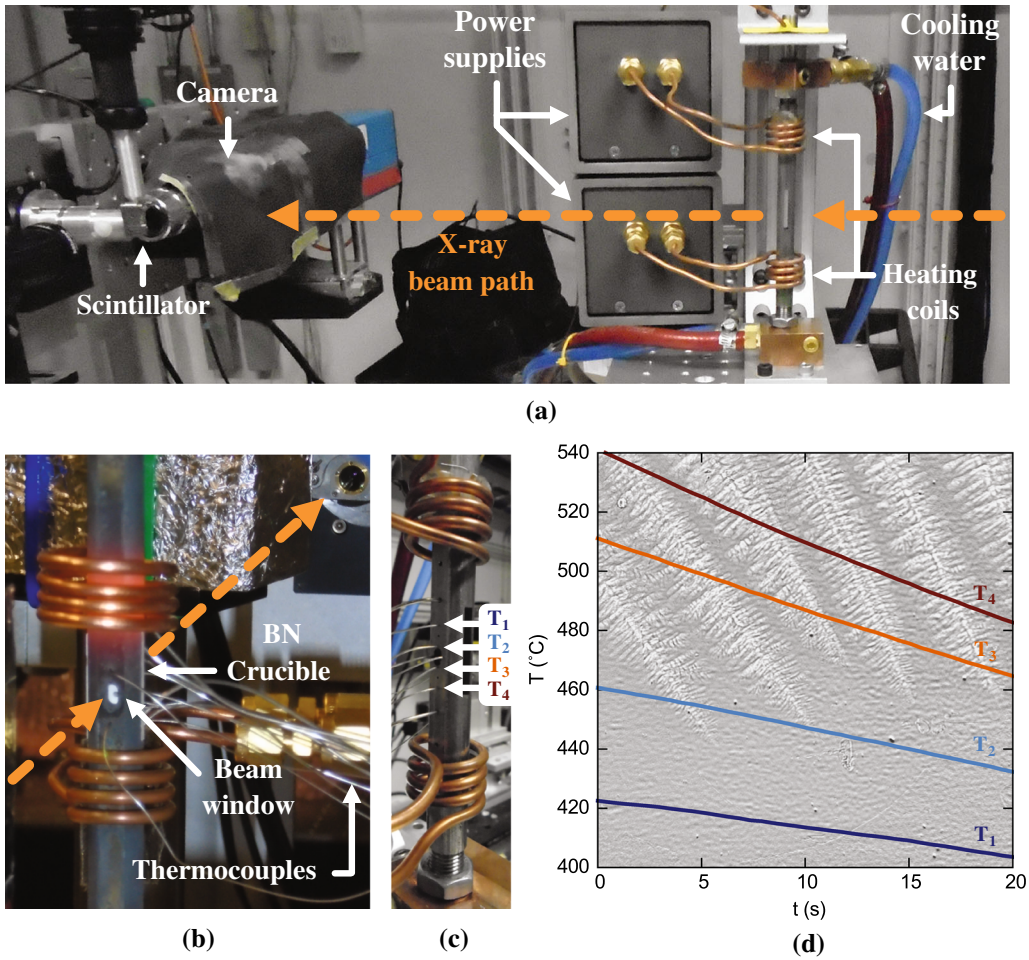

Fig. 1—Directional solidification furnace setup installed at Argonne National Laboratory's Advanced Photon Source. (*a*) shows the induction furnace with an empty steel rod. The heated steel rod in (*b*) contains a boron nitride (BN) crucible with a partially melted sample. (*c*) provides a detailed view of the thermocouples, and (*d*) shows the temperature evolution measured by four of these thermocouples as the dendrite front swipes through the field-of-view for the specific sample discussed throughout the article. Note that, unlike in (b), the solidification of this sample proceeds from the top downward, as in the background image of (d), *i.e.*, with $T_1 < T_2 < T_3 < T_4$.

between the readings of the two thermocouples directly above and below the observation window (respectively labeled T_2 and T_3 in Figure 1(c)) divided by the distance between them (6.0 mm). The resulting measured values at the location of the sample were a temperature gradient of $G = 6.68$ K/mm and a cooling rate of $\dot{T} \approx -1.89$ K/s (Figure 1(d)). With a thermocouple accuracy of the order of ± 2 K, the errors on G and $\dot{T}$ are of the order of 0.7 K/mm and 0.25 K/s, respectively.

3. *In situ solidification radiography*

To provide a low attenuating pathway for *in situ* synchrotron X-ray imaging, the steel rod of the furnace had a central hole, about 1.6 mm in diameter, running trans-axially through the rod, perpendicular to the foil sample. The crucible also had a 1 mm diameter through hole aligned with the rod's through hole (Figure 1(b)). While the sample was melted, the aluminum oxide surface layer and surface tension of the melt prevented the alloy from pouring out of the crucible through the X-ray window.

The furnace setup was installed at the Sector 32 Insertion Device beamline at Argonne National Laboratory's Advanced Photon Source (APS) for imaging with a pink X-ray beam with a peak intensity at 25.7 keV. X-rays passed through the metal alloy sample and impinged upon a 30 μm thick LuAG:Ce scintillator where they were converted to visible light. A mirror was positioned behind the scintillator that reflected the images to a movie camera (Figure 1(a)). The resulting radiograph field-of-view at the sample was 1.075 mm $\times$ 1.344 mm with a pixel size of 1.05 μm. The detector exposure was set at 5 ms with a frame rate of 5.3 Hz.

4. *Solidification modeling*

We simulate the solidification of our thin Al-12 at. pct Cu sample with a multi-scale dendritic needle network (DNN) model in three dimensions (3D).[75] The model avoids explicitly tracking the complex morphological features of the solid–liquid interface. This permits using a numerical grid size of the same order as the typical dendrite tip radius, which is about one order of

magnitude larger than what is required using phase-field modeling. Using explicit finite differences, this results in calculations up to four (in 2D) or five (in 3D) orders of magnitude faster than using phase-field, and hence allows simulating large dendritic arrays with tens of thousands of dendrites at experimentally relevant length and time scales. The current model considers a purely diffusive growth regime, which might not exactly be the case in the experiments due to gravity-induced thermo-solutal convection.[11,76–78] However, convection effects being for the most part limited to low growth velocities,[11] in the well-developed dendritic regime the model can quantitatively predict microstructural features, such as dendritic spacings, as previously shown for various Al-based alloys in thin samples experiments.[75,79,80]

As detailed in References 74 and 75, the DNN approach consists of tracking the evolution of a network of parabolic needles growing and interacting through a solute field transported within the liquid. For directional solidification conditions,[74,75] we use the frozen temperature approximation $T = T_0 + G(z - V_p t)$, where T_0 is a chosen reference temperature (here the solidus temperature of the alloy) and V_p is an equivalent "pulling" velocity calculated as $\dot{T}/G$, and directed along the z direction. The solute field c follows

$$\frac{\partial c}{\partial t} = D\nabla^2 c \qquad [1]$$

in the liquid, and $c = c_i$ with

$$\frac{c_i}{c_l^0} = 1 - (1-k)\frac{z - V_p t}{l_T} \qquad [2]$$

along the needle network. Eq. [1] can be substituted by any transport equation—here only diffusion with a solute diffusivity D is considered. Eq. [2] stands for thermodynamic equilibrium, *i.e.*, the Gibbs–Thomson condition, along the solid–liquid interface, with interface curvature neglected at the scale of the entire needle network. The reference concentration c_l^0 is that of a planar interface at the reference—*i.e.*, solidus—temperature T_0, k is the solid–liquid interface partition coefficient, and $l_T = m(k-1)c_l^0/G$ is the thermal length—*i.e.,* the distance between liquidus and solidus temperatures—with $m < 0$ the alloy liquidus slope. Kinetic undercooling and solid-state diffusion are neglected.

The growth of each needle is integrated with time following two conditions that uniquely prescribe the evolution of its tip radius ρ and tip velocity V. The first condition established at the scale of the dendrite tip radius is the microscopic solvability condition.[81]

$$\rho^2 V = \frac{c_l^0}{c_i}\frac{2Dd_0}{\sigma^*}, \qquad [3]$$

where $d_0 = \Gamma_{sl}/[m(k-1)c_l^0]$ is the solute capillarity length with Γ_{sl} the interface Gibbs–Thomson coefficient, and σ^* is the tip selection constant. The prefactor on the right-hand-side of Eq. [3] stands for the temperature dependence of the capillarity length, since d_0 is expressed at the reference temperature T_0 of the solidus. The second condition is established at an intermediate scale much larger than the tip radius, but much smaller than the diffusion length. (Since the model is valid for low Péclet number applications, we have $\rho \ll D/V$.) At this scale the solute conservation of a shape-preserving paraboloid growing at a quasi-steady velocity V can be written as[75]:

$$\rho V = \frac{c_l^0}{c_i} D\mathcal{F}, \qquad [4]$$

where the flux intensity factor $\mathcal{F}$ measures the incoming solute flux over a length a behind the tip and is defined as

$$\mathcal{F} \equiv -\frac{1}{(1-k)c_l^0}\frac{1}{2\pi a}\iint_{\Gamma'}\frac{\partial c}{\partial n}d\Gamma' \qquad [5]$$

with n the outward normal to the surface Γ', *i.e.*, to the solid–liquid interface, over a length a. This flux intensity factor can be integrated using any surface Γ, with an enclosed liquid volume Σ that intersects the considered needle tip at a distance a behind the tip (see Figure 2(b) in Reference 75) using,

$$\iint_{\Gamma'}\frac{\partial c}{\partial n}d\Gamma' = \iint_{\Gamma}\frac{\partial c}{\partial n}d\Gamma + \frac{V}{D}\iiint_{\Sigma}\frac{\partial c}{\partial z}d\Sigma. \qquad [6]$$

The growth of each individual needle is thus integrated over time by combining Eqs. [3] and [4] to solve for $\rho(t)$ and $V(t)$. While the solvability condition [3] yields the constancy of the product ρV^2, the solute balance at intermediate scale [4] incorporates the time evolution of the solute field surrounding the tip through the time dependent flux intensity factor $\mathcal{F}(t)$. Reformulating Eqs. [3] through [4] as a function of a normalized solute field $u \equiv (c_l^0 - c)/[(1-k)c_l^0]$ directly yields Eqs. [40] and [42] from Reference 75. Further details on the model and its implementation can be found in References 74 and 75.

The inputs of the simulation are the alloy and process parameters. For the alloy, the nominal concentration is $c_0 = 12$ at. pct Cu (*i.e.,* 24.3 wt pct Cu), the solid–liquid interface solute partition coefficient is $k = 0.17$,[82] the liquidus slope is $m = -3.4$ K/wt pct Cu,[83] the solute diffusion coefficient in the liquid is $D = 3.5 \times 10^{-9}$ m^2/s[84] (diffusion in the solid phase is neglected), the Gibbs-Thomson coefficient of the interface is $\Gamma_{sl} = 2.36 \times 10^{-7}$ Km,[85] and the tip selection parameter is $\sigma^* = 0.06$ (representing a surface energy anisotropy of $\varepsilon_4 \approx 0.012$ for a one-sided model[81,86]). Discussions of the parameters for Al-Cu alloys and corresponding uncertainties can be found in previously published papers, *e.g.* Reference 11. The processing parameters are a temperature gradient $G = 6.68$ K/mm and a velocity of the isotherms (or equivalent "pulling" velocity) $V = 283\,\mu$m/s, set to match the experimental measurements of the temperature gradient and cooling rate $\dot{T} \approx -1.89$ K/s at the center of the sample.

The total simulation size is approximately $2.51 \times 1.99 \times 0.10$ mm^3 (*i.e.,* half of the sample thickness) over one minute, which corresponds to a representative subset of the experimental domain of $\approx 30 \times 11 \times 0.2$ mm^3. All

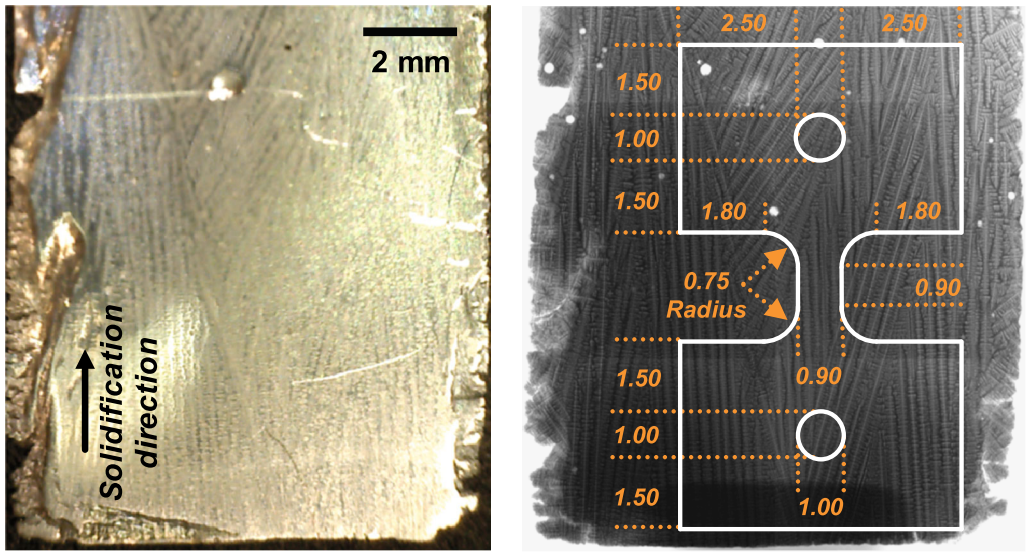

(a) (b)

Fig. 2—Directionally solidified sample: (*a*) surface image and (*b*) microfocus X-ray radiograph, showing the location, geometry, and dimensions of the laser-cut tensile specimen (in mm).

boundaries are set to no-flux symmetry planes. In order to mimic an initially planar interface, the initial state consist of 154 closely packed needles parallel to the temperature gradient direction with their tip aligned at the liquidus temperature location. Even though the number 154 is mostly arbitrary, it was chosen high enough to start with an initial spacing ($< 13\,\mu$m) small enough to trigger substantial competition and elimination among primary dendrites, all while ensuring minimal influence of the no-flux boundary conditions (*i.e.,* starting with 1/2 of the initial spacing between the two needles on the outer sides of the initial array and the boundaries). A small random perturbation on the order of 10^{-6} times the steady tip radius was added to the individual initial length of the needles in order to disturb the initial symmetry. The finite difference cubic grid size is $\Delta x = 1.0\,\mu$m (*i.e.*, about 0.89 times the theoretical steady state dendrite tip radius for these conditions). The explicit time step is set to $\Delta t = \Delta x^2/(6D) \approx 4.76 \times 10^{-5}$ s. We simulate a dendritic grain growing tilted by 30 deg with respect to the temperature gradient direction in order to match the X-ray radiography observations (see Section III–A–1). To do so, we keep the dendritic branches aligned with the numerical grid and actually tilt the isotherms.[79] The most advanced tip location is kept at a distance of 187 μm from the far-ahead liquid boundary (*i.e.* over 15 times the steady diffusion length D/V). The solute flux integration box around each needle tip spans $3\Delta x$ ahead and behind the needle tip, and is one Δx wider than the needle thickness $3\Delta x$ behind the tip. The thickness (radius) of the needles is bound to 4 times the steady tip radius of the free dendrite. Sidebranching frequency is set to occur every time a needle grows by a length of between 10 and 20 times the steady state tip radius (see Reference 75 for a detailed definition and discussion of all numerical parameters).

B. *Microstructure*

1. *Specimen extraction*

The solidified sample was removed from the furnace assembly, mounted with adhesive, mechanically ground to remove surface oxide, and then released from the mount with acetone. The foil was then attached to a glass microscope slide as a mechanical support with adhesive. Tensile coupons were laser machined out of the foil. The tensile coupons and the surrounding foil were then removed from the mechanical support by dissolving the adhesive with acetone.

The current article focuses on the analysis of one of the resulting microscale tensile specimen, illustrated in Figure 2. The location of the tensile sample corresponds to a region with primary dendrites well aligned with the temperature gradient direction, *i.e.*, with the loading direction of the tension tests. Thus, the sample had a gauge length oriented approximately parallel to the primary dendritic trunks (Figure 2(b)), larger grip ends with pin holes, and filets at the grip-gauge section intersections.

2. *Microtomography*

We characterized the microstructure within the tensile sample using microscopic computed tomography (micro-CT), with a Carl Zeiss microfocus X-ray CT system. Imaging was conducted with a Hamamatsu X-ray source operating at 80 kV and 10 W. The X-ray detector for imaging was configured with a scintillator crystal lens-coupled to a CCD camera, using a 10× objective and a right-angle mirror to divert light away from the X-ray path. The center of rotation was placed 45 mm from the X-ray anode, and the scintillator crystal was placed 60 mm from the X-ray anode, resulting in a 1.33× geometric X-ray magnification. The result of the imaging configuration was a 2 mm × 2 mm field-of-view

with an effective pixel size of 2.0 μm. For the CT scan of each sample, 2001 equally spaced X-ray projection images were acquired over 184 deg to compensate for the angle of the X-ray cone beam. A 35 second exposure time was used for each X-ray image, and background images were acquired before, after, and intermittently throughout the CT scans. The tomogram reconstructions from the sets of X-ray radiographs were performed with a beam-hardening correction *via* the TXMReconstructor software package, using cubic reconstruction voxels of 2.0 μm edge length. The tomograms then provided a grayscale representation of the sample three-dimensional geometry and microstructure in terms of the effective attenuation within each voxel.

The tomograms were segmented with a grayscale threshold into three distinct phases: the surrounding air, the eutectic structure, and the proeutectic Al-rich phase with a dendritic morphology. To reduce segmentation artifacts at the surface from laser machining, the air phase surrounding the sample was dilated volumetrically by five voxels. Then, the solid phases were dilated volumetrically by five voxels, but only at the surface. Tomogram visualization and image processing, including alignment, cropping, and segmentation, were performed using the AvizoFire v9.1 software.

C. *Mechanical Properties*

1. *Tensile testing*

We used a CT500 micromechanical testing systems from Deben UK Ltd to measure the tensile response of the sample. This setup also enabled *in situ* radiography during testing, using the lab-scale Carl Zeiss X-ray CT system.

The sample was loaded into the base grip by lowering it between the grip faces and inserting the steel pin. The sample was supported in the upright position, while the lower grip was softly clamped. The top grip was then lowered over the upper grip section of the sample until the grip pin holes aligned with the sample hole. With both pins in place, the grips were driven apart until a slight increase in load was detected, and the load was then released to zero by driving the grips back together. Then, with the pins assumed to be in position, the upper and lower grips were clamped firmly on the sample.

This system recorded the load and displacement of the sample at a rate of 10 Hz. Even at the slowest displacement rate for the system, 0.1 mm/min, we used a high imaging frame repetition with frame rate of 1 Hz. To compensate for the resulting low imaging signal, a high binning factor was used. The combined detector and geometric X-ray magnification was 13× and the detector acquired with 4 × 4 pixel binning, yielding an effective pixel size of 4.1 μm. The sample was tested in displacement control at a rate of about 0.1 mm/min.

The as-solidified segmented CT scan was used for calculating the engineering stress. More precisely, the cross-sectional area was measured from each voxelized plane perpendicular to the loading direction in the segmented CT volume. Then, the engineering stress was calculated from each recorded load data point during tensile testing. The engineering strain was calculated using the displacement values at each recording point and the average initial gauge length of the samples as measured from the tomogram images. The elastic modulus, E, was measured using the slope of the line of best fit up to 1 pct strain. The ultimate tensile strength, σ_{UTS}, was defined as the stress calculated for the minimum cross-sectional area at the maximum recorded load. The yield stress, σ_Y, was defined using 0.2 pct deviation from linearity. Strain-to-failure, ε_f, was measured during the steep stress decrease as the strain at the first point below 10 pct of the UTS.

2. *Fracture nanotomography*

Fracture surface imaging was performed with 150 nm spatial resolution X-ray nano-CT using a Carl Zeiss UltraXRM 500 system. A roughly 60 μm diameter, 100 μm tall micropillar was mechanically lathed from the fracture zone of one half of a Al-12 at. pct Cu after tensile failure, with the top surface located along a portion of the fracture surface. Several gold spheres 3 μm in diameter were adhered to the micropillar, and one of the spheres was positioned at the center of rotation of the nano-CT setup to aid in X-ray projection alignment for reconstruction.

X-ray imaging was conducted with a Cu anode at 1.2 W, primarily using the Cu Kα edge at 8.04 keV for imaging. The X-ray detector consisted of a 1024 × 1024 CCD camera lens coupled to a scintillator crystal. The effective size of the detector pixel with respect to the sample volume was configured at 65 nm. Over 180 deg of sample rotation 701 angularly distinct, uniformly separated attenuation contrast radiographs were acquired, and background images were acquired before and after sample imaging, with an exposure time of 100 seconds for each image. The projections were then aligned using Carl Zeiss Xradia Align. The radiographs were then calculated with the sample projections and the background images, and the tomogram of the micropillar containing the tensile fracture surface was calculated using the TXMReconstructor software package.

3. *Mechanical modeling*

The micromechanical response of the Al-12 at. pct Cu specimen was simulated using the EVPFFT model. It is a full-field crystal plasticity approach able to be directly applied to voxelized microstructure images. The formulation has been thoroughly described elsewhere;[65] therefore, here we only provide a compact description of its main characteristics.

FFT-based models operate on a regularly spaced grid of computational/material points, representing a sampling of the material's properties, such as voxelized images obtained by micro-CT, or synthetic microstructures obtained by means of microstructure evolution modeling techniques, *e.g.*, phase-field.[87] Upon convergence, EVPFFT gives the stress and strain fields at each grid point x that fulfills equilibrium and compatibility, respectively, and the local stress–strain constitutive relation. The small-strain EVPFFT model combines elastic and viscoplastic constitutive descriptions and an Euler implicit time discretization, to give:

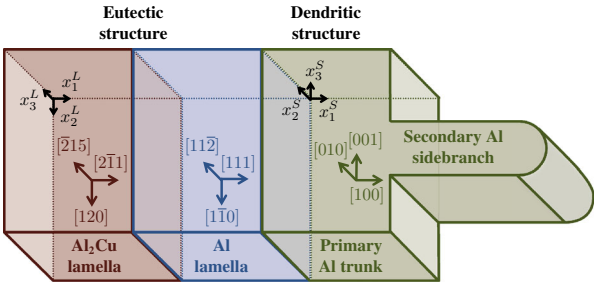

Fig. 3—Schematics of the assumed morphology and orientation relationships between the Al dendritic and Al/Al_2Cu eutectic phases and within the Al/Al_2Cu eutectic structure.

$$\varepsilon(x) = \varepsilon^e(x) + \varepsilon^p(x) = C^{-1}(x) : \sigma(x) + \varepsilon^{p,t}(x) + \dot{\varepsilon}^p(x,\sigma)\Delta t, \quad [7]$$

a constitutive relation for time $t + \Delta t$ that relates the total local strain $\varepsilon(x)$, given by the sum of the elastic $\varepsilon^e(x)$ and plastic $\varepsilon^p(x)$ strain components, with the corresponding stress field $\sigma(x)$. In Eq. [7], $C^{-1}(x)$ is the local elastic compliance, $\varepsilon^{p,t}(x)$ is the plastic strain at time t, and $\dot{\varepsilon}^p(x,\sigma)$ is the plastic strain rate, constitutively related with the stress through the single-crystal plasticity relation:

$$\dot{\varepsilon}^p(x) = \sum_{s=1}^{N} m^s(x)\dot{\gamma}^s(x) = \dot{\gamma}_0 \sum_{s=1}^{N} m^s(x)\left(\frac{\left|m^s(x) : \sigma(x)\right|}{\tau^s(x)}\right)^n sgn\left\{m^s(x) : \sigma(x)\right\}, \quad [8]$$

where N is the number of active slip systems; $\dot{\gamma}^s(x)$, $\tau^s(x)$, and $m^s(x)$ are, respectively, the shear rate, the critical resolved shear stress (CRSS), and the Schmid tensor associated with slip system (s)—a function of the crystallographic orientation of the single-crystal material point; $\dot{\gamma}_0$ is a normalization factor, and n is the stress exponent. In order to account for strain hardening, at the end of each time increment the local CRSSs are updated based on the calculated plastic slip. We use here a generalized Voce hardening law given by:

$$\Delta\tau^s = \frac{d\overline{\tau}^s}{d\Gamma}\sum_s h^{ss'}\Delta\gamma^{s'} \quad [9]$$

$$\overline{\tau}^s = \tau_0 + (\tau_1 + \theta_1\Gamma)\left[1 - \exp\left(-\frac{\theta_0\Gamma}{\tau_1}\right)\right], \quad [10]$$

where $\Delta\tau^s$ is the CRSS increment on slip system (s), $\Delta\gamma^{s'}$ is the shear increment on system (s'), $h^{ss'}$ is the latent hardening matrix that dictates how slip activity in different slip systems harden each other, Γ is the accumulated slip over all slip systems, and τ_0, τ_1, θ_0, and θ_1 are calibrated parameters.

EVPFFT simulations were carried out directly on the voxelized experimental sample geometry from the microstructure obtained by segmentation of the micro-CT images of the tensile Al-12 at. pct Cu specimen, imposing uniaxial tension along sample direction 3 (x_3^S), with Voce hardening parameters calibrated to match the yield stress and final stress measured from the experiment. In order to reduce the effect of possible noise at the sample surface, the microstructure used in the simulation has half the resolution of the original image, resulting in a $343 \times 90 \times 490$ voxel grid. Since micro-CT images could not fully resolve the two-phase eutectic lamellar structure, in first approximation, the eutectic was treated as a lamellar matrix surrounding the dendritic structure, with a set orientation of each phase and of the lamellae. Thus, the following assumptions were made, in terms of morphology, orientation relationships, local elastic and plastic properties of the phases (see Figure 3).

Dendritic structure Since the primary dendrites in the tested specimen were aligned with the tensile loading direction, the Al dendritic phase was assumed to have a single crystallographic orientation, namely with [001] crystallographic direction along the tensile axis. The dendritic phase has mildly anisotropic Al single-crystal (cubic) elastic constants: $C_{11} = 108$ GPa, $C_{12} = 62$ GPa, $C_{44} = 128$ GPa,[88] expressed in sample axes (x_1^S, x_2^S, x_3^S), and deforms plastically by $\{111\}\langle 110\rangle$ slip, comprising 12 slip systems with identical CRSS.

Eutectic structure The two-phase Al/Al_2Cu eutectic structure is modeled as a homogenized material, with elastic properties given by the combined elastic response—accounting for the lamellar morphology—of the strongly orientation-correlated fcc Al and tetragonal Al_2Cu lamellae, and plastic properties given by plastic accommodation in the fcc Al phase by $\{111\}\langle 110\rangle$ slip affected (*i.e.,* strengthened) by the lamellar morphology and the presence of the plastically hard intermetallic phase. Figure 3 shows the geometry/orientation correlations underlying the aforementioned homogenization assumptions: (a) the [111] direction of the Al lamellae parallel to the [100] direction of the dendritic phase, *i.e.*, perpendicular to the primary dendrite orientation; (b) an orientation relationship between Al and Al_2Cu lamellae of the type beta-6,[89,90] *i.e.*, with common plane (111) Al // $(2\bar{1}1)$ Al_2Cu // lamellar plane, and common direction $[\bar{1}10]$ Al // [120] Al_2Cu. The homogenized elastic properties for the eutectic matrix were obtained by performing an elastic self-consistent calculation[91] for the representative 2-lamellae microstructure shown in Figure 3, with elastic constants for Al (cubic) from Reference 88 given above, and for Al_2Cu (tetragonal) $C_{11} = 164$ GPa, $C_{33} = 246$ GPa, $C_{12} = 78$ GPa, $C_{13} = 15$ GPa, $C_{44} = 34$ GPa, $C_{66} = 37$ GPa,[92] resulting in the following elastic stiffness tensor for the eutectic phase expressed in lamellar axes (x_1^L, x_2^L, x_3^L) with (mild) triclinic symmetry:

$$C_{ij} = \begin{bmatrix} 126 & 63 & 57 & 0 & -4 & 0 \\ 63 & 133 & 49 & 0 & -8 & -1 \\ 57 & 49 & 145 & 0 & 15 & 0 \\ 0 & 0 & 0 & 31 & 0 & -2 \\ -4 & -8 & 15 & 0 & 37 & 0 \\ 0 & -1 & 0 & -2 & 0 & 31 \end{bmatrix} GPa \quad [11]$$

As consequence of the orientation relationship and the harder plastic behavior of the intermetallic phase,[93] the homogenized plastic properties of the eutectic phase were assumed to be (similarly as in Reference 94 for a TiAl lamellar structure): (a) soft slip, $\tau^s = \tau^s_{soft}$ in Eq. [8], on the 3 $\{111\}\langle 110\rangle$ systems with slip plane parallel to the (111) lamellar plane, and (b) hard slip, $\tau^s = \tau^s_{hard} = 4 \times \tau^s_{soft}$, of the other 9 $\{111\}\langle 110\rangle$ slip systems. The ratio 4 between hard and soft slip systems was kept fixed throughout the calculation, as the eutectic structure hardened. The dependence of mechanical properties of the eutectic structure upon its lamellar spacing,[93] which as a first approximation we chose not to account for here, could be included by tuning this ratio between hard and soft slip systems.

The above idealized assumptions are likely to introduce some level of uncertainty in the local (*i.e.* at voxel level) micromechanical predictions. However, since the goal of the present modeling is to establish statistical correlations between averaged micromechanical fields in the regions of the sample of high curvature and the location of fracture initiation (see Section IV–B) the voxel-level errors are expected to average out.

III. RESULTS

A. *Processing*

1. *In situ solidification radiography*

Radiography images captured during the solidification of the Al-12 at. pct Cu alloy at $G \approx 6.68$ K/mm and $\dot{T} \approx -1.89$ K/s are shown in Figure 4. Dendrites grow with an angle of about 30 deg with respect to the (vertical) temperature gradient direction. The images show two different grains with a small misorientation. The presence of the converging grain boundary (GB) toward the left of the image leads to the elimination of one dendrite in the most misoriented dendritic array (Figures 4(c) and (d)). The overlapping traces of the two grains at the GB in Figure 4(d) suggests additional degrees of three-dimensional misorientation of the two grains. Additionally, one of the primary dendritic trunks of the grain most favorably oriented with the temperature gradient breaks (toward the right of the image), possibly due to the stress induced by the impingement of the neighboring dendrite at the near converging GB. The average primary spacing, calculated by averaging three horizontal measurements at the bottom, center, and top of the final solid microstructure, is $\lambda_1^{\text{Exp}} \approx 185 \pm 14\,\mu$m, expressed in the direction normal to the primary trunks growth axis (*i.e.*, tilted by about 30 deg from the horizontal axis).

2. *Solidification modeling*

Figure 5 shows snapshots of the corresponding DNN simulation. Shortly after the destabilization of the pseudo-planar interface (at the top of Figure 5(a)), a fast, hierarchical elimination of several generations of primary dendrites occurs. Hence, about $t = 10$ second after the start of cooling (Figure 5(a)), most initial needles have stopped growing and a primary spacing has already been selected. At $t \approx 15$ second, the dendritic front approaches a value close to its final undercooling $\Delta \approx 0.0275$ (defined as the distance between the solidification front and the liquidus isotherm normalized by the distance between solidus and liquidus isotherms). Then, the elimination of additional primary dendrites proceeds at a much slower time scale, as illustrated by the visible elimination of a single primary dendrite between $t =$ (b) 16 and (c) 60 second. The two mechanisms responsible for dynamical primary spacing evolution are illustrated in Figure 5(d) (at $t = 22$ second), namely: (E) local increase of spacing by primary dendrite elimination, and (B) local decrease of spacing by tertiary branching. Unlike in the experiment of Figure 4, the DNN simulation involves only one grain. However, Figures 5(a) through (c), represented at the same scale as Figure 4, show similar microstructural features as in the experiments, with a final average primary spacing $\lambda_1^{DNN} \approx 223\,\mu$m and a distribution within $244 \pm 95\,\mu$m. Hence, while the average predicted spacing is higher than the average measurements by about 20 pct, the latter falls within the predicted steady distribution range.

B. *Microstructure*

X-ray micro-CT characterization of the tensile specimen revealed three distinct phases within the tomogram, as illustrated in Figure 6. The lowest attenuating phase of the tomogram is the air surrounding the sample, revealing the overall geometry of the tensile specimen. The moderately attenuating phase is the Al-rich phase, present throughout the sample with a dendritic morphology. The highest attenuating region, rich in copper, is the ($Al_2Cu + Al$) eutectic structure, surrounding the Al-rich dendrites throughout the sample. As expected from visual assessment of the sample surface, most primary Al dendrite axes are well aligned with the gauge length, and hence with the stress direction in tension.

The micro-CT tomograms were segmented by applying an intensity threshold followed by surface cleaning steps. Figure 7 illustrates a single slice as the original grayscale (a) and the segmented (b) tomogram volume. In the latter, the black region corresponds to the air, the magenta region corresponds to the eutectic, and the green region corresponds to proeutectic Al-rich dendrites. Figure 7(c) shows a three-dimensional rendering of the internal microstructure, with the surrounding air shown as fully transparent, the eutectic structure shown as transparent light purple, and the proeutectic Al-rich phase shown as opaque green.

In addition to 3D rendering for visual inspection, the segmented microstructure was useful on several fronts. Firstly, the voxel count provides a direct measurement of the volume fraction of dendritic and eutectic structures, here, respectively, measured at $g_D \approx 0.32$ and $g_E \approx 0.68$. These fractions are close to those obtained using a simple analytical Gulliver-Scheil approximation, $g_E = (c_0/c_E)^{\frac{1}{1-k}} \approx 0.70$, using a nominal concentration

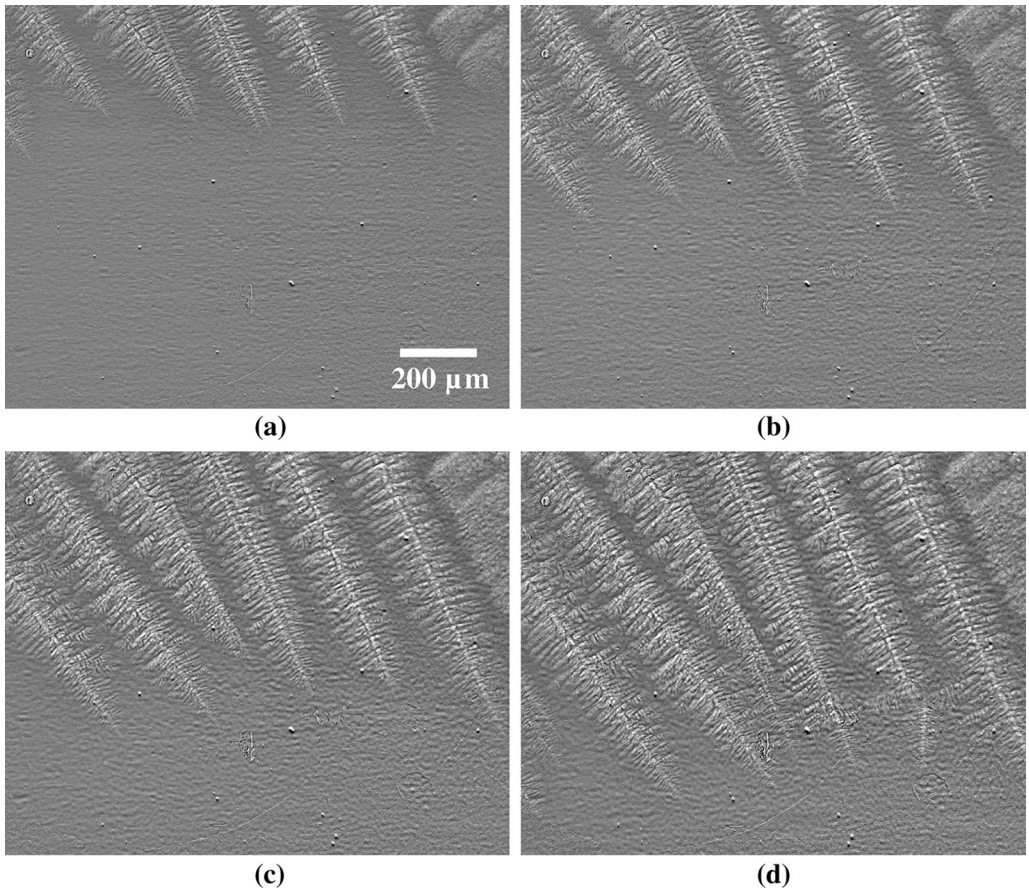

Fig. 4—Synchrotron X-ray radiographs acquired during solidification of the Al-12 at. pct Cu sample, showing Al-rich dendrites growing from the top downward. Images (*a*) through (*d*) are 20 imaging frames, *i.e.*, about 3.77 s, apart from each other.

$c_0 = 24.3$ wt pct Cu, a eutectic concentration $c_E = 32.7$ wt pct Cu and a solute partition coefficient $k = 0.17$.[82] Secondly, the segmented micro-CT tomograms can be used to analyze the phase homogeneity across the cross-sections of the gauge length within the sample. The volume fractions of dendritic and eutectic structures through normal cross sections along the the gauge length has a standard deviation of 0.037, illustrating the relative homogeneity of the sample along its principal direction. Finally, the segmented dendrite microstructure is also used to directly input the experimental microstructure into mechanical simulations.

C. *Mechanical Properties*

1. *Tensile testing*

in situ X-ray radiographs acquired during tensile testing are shown in Figure 8. The primary interest with *in situ* X-ray imaging of the test testing was attempting to capture dynamic fracture events in the microstructure. However, a 1 Hz imaging frequency was not sufficient to capture crack propagation steps. Approximately 20 seconds into the loading, the sample is still intact and neither cracking nor voiding can be observed (Figure 8(b)). However, 1 second later, *i.e.*, at $t \approx 21$ second, the sample has reached total failure (Figure 8(c)). The fracture appears to have propagated through the sample following a relatively straight path, without any major branching or bridging of the crack. Further detailed characterization of the fracture path appears in Section III–C–3, using higher resolution 3D characterization.

The resulting experimental stress–strain curve is given in Figure 9 (thin red line). Corresponding mechanical properties (discussed later in Section IV–C) are: elastic modulus $E = 4.2$ GPa, ultimate tensile strength $\sigma_{UTS} = 120$ MPa, yield stress $\sigma_Y = 59$ MPa, and strain-to-failure $\varepsilon_f = 4.9$ pct.

2. *Fracture imaging*

Nano-CT imaging of a representative portion of the tensile fracture surface is shown in Figure 10. The black area corresponds to air, and the large clustered dark gray regions are Al-rich dendrites. The two-phase eutectic structure appears as a mix of light gray and dark gray regions, corresponding to Al_2Cu and Al, respectively. The nano-CT tomogram, with a spatial resolution of roughly 150 nm, shows the fracture pathway more clearly than is possible with micro-CT, even revealing details of the the two phases within the eutectic.

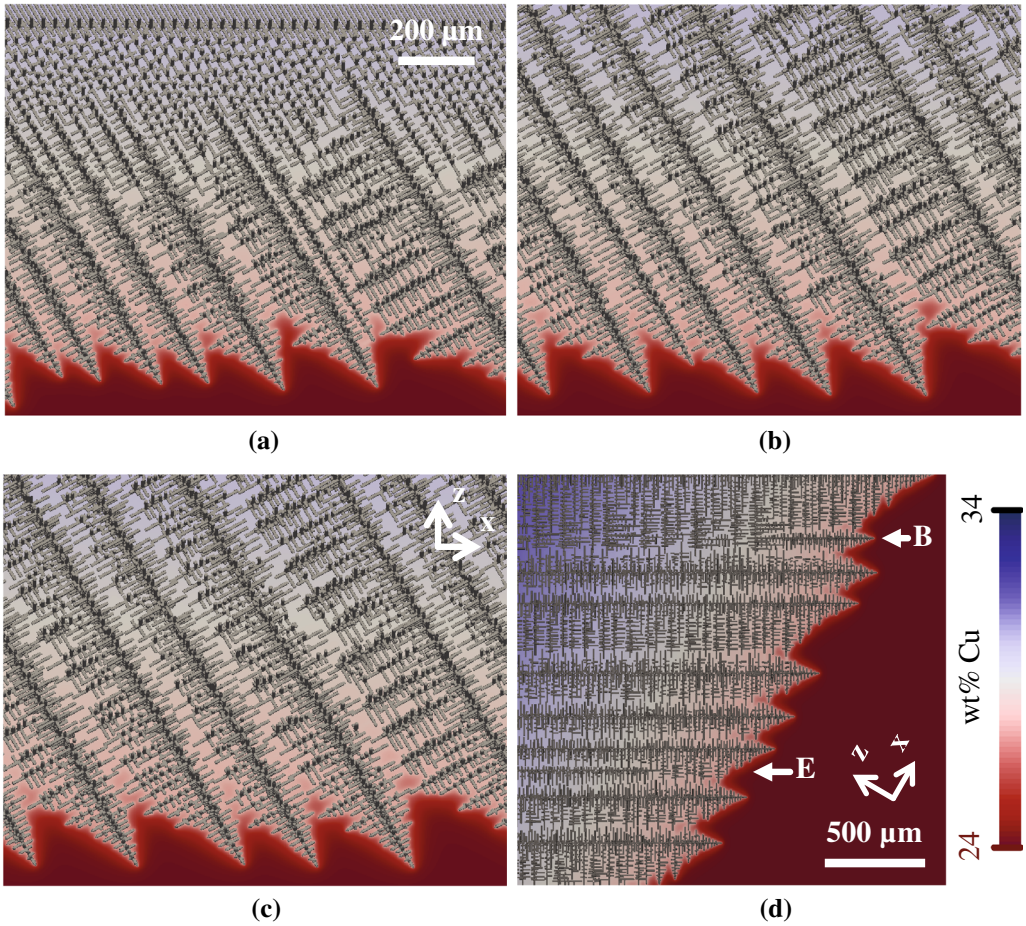

Fig. 5—Microstructure growth in the Al-12 at. pct Cu sample simulated with the 3D DNN model, showing dynamical spacing selection after (*a*) 10, (*b*) 16, and (*c*) 60 s of cooling. The snapshot in (*d*), after about 22 s of cooling, illustrates the two main mechanisms of spacing selection, namely reduction of spacing by tertiary branching (B) and spacing increase by primary dendrite elimination (E).

3. *Mechanical modeling*

To simulate the mechanical loading, the deformation rate of 0.1 mm/min described in Section II–C–3 is applied to the microstructure image over the time duration of the loading until failure. Using these loading conditions, the Voce hardening parameters from Eq. [9] are fit such that the yield stress and final stress of the simulation matches the measured yield stress and failure stress. The final Voce parameters are 53, 10, 682, and 680 MPa for τ_0, τ_1, θ_0, and θ_1, respectively. Figure 11 shows the resulting local von Mises equivalent stress and strain distributions, extracted from the local tensors at each point in the microstructure. The von Mises stress averages at 120 MPa within the dendritic phase and 123 MPa in the eutectic structure, and the average von Mises strain is 0.0281 in the dendritic phase and 0.0266 in the eutectic. The overall calculated stress–strain curve appears in Figure 9 (thick blue line).

Figure 11(a) shows that the widest variation of stress occurs within the eutectic, with a dendritic structure essentially appearing in the gray range of values around 125 MPa. The strain distribution in Figure 11(b) shows highest values located in the four regions where the sample geometry exhibits a high curvature. These four regions are marked with circles and labeled I through IV in Figure 11(b). In Section IV–C, we analyze and discuss different stress and strain states within each of these regions, namely accounting for voxels within the cylinder of axis normal to the main sample plane and intersecting the sample center plane along the circles shown in Figure 11. Within these regions, we estimate the average von Mises equivalent stress and strain, the hydrostatic stress, and the elastic and plastic strain energies. The energy terms are found by performing a numerical time integration of the inner product of the stress tensor with the elastic and plastic strain rates, respectively, over the duration of the simulation. The distributions of these terms within each volume take the form of similarly spread normal distributions. As such, the mean of the distributions, shown in Table I, may be used to compare the regions with one another.

IV. DISCUSSION

A. *Processing*

Comparisons between directional solidification experiments (Figure 4) and DNN simulations (Figure 5) show a good agreement on selected microstructural

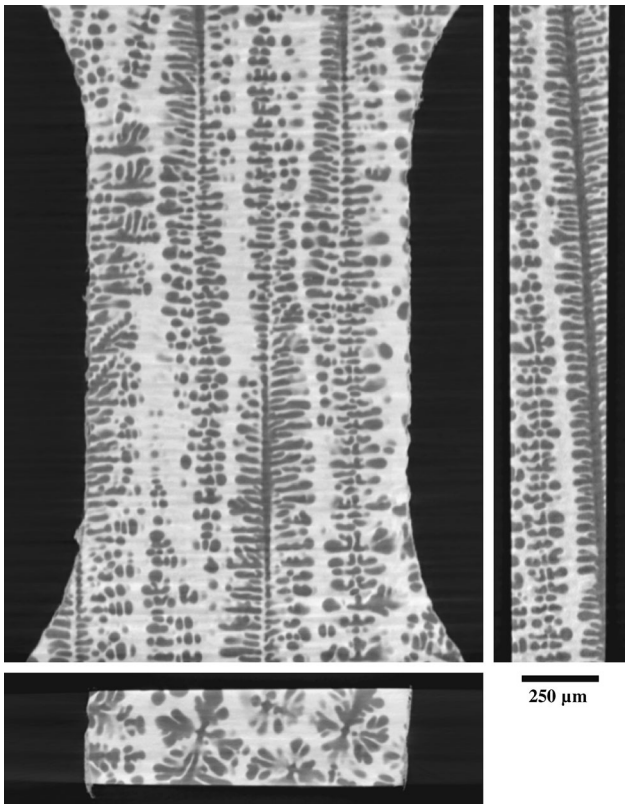

Fig. 6—Orthogonal cross-sections of the micro-CT tomograms showing the dendritic microstructure in the gauge length of the tensile specimen.

length scales, with a predicted value of the average primary spacing, λ_1, within 20 pct of the measured value, and a significant overlap of the measured and simulated spacing distributions around 200 μm.

The 3D DNN simulation is widely multi-scale, combining fundamental mechanisms taking place at the scales of the stationary tip capillarity length $d_0^* = 3.1$ nm, the typical stationary dendrite tip radius $\rho_s = 1.13\,\mu$m, the solute diffusion length $l_D = 12.4\,\mu$m, and the thermal length $l_T = 60.4$ mm (see Reference 75 for a detailed definition of those terms). This separation of scales would make the simulation of just a few dendrite tips up to a steady growth using phase-field extremely challenging, if feasible at all. In our DNN calculation, the total number of needles peaks around 21250 at $t \approx 19$ second and slowly decreases to stabilize around 20500 after $t \geqslant 40$ second. The simulation of the $2.5 \times 2.0 \times 0.1$ mm^3 domain over 60 second was performed in 14 days on a single Nvidia Tesla K40c graphics processing unit.

In the context of the current study, the DNN approach also presents some limitations. Its main shortcoming stems from the fact that it is aimed at accurately simulating the concurrent growth of dendrite tips into the liquid phase, but does not accurately describe late-stage solidification at high solid fraction. Therefore, the main output of the model is a dendritic "skeleton," but not a fully solid microstructure that could be directly used as input of a micromechanical model. Despite this limitations in modeling late-stage solidification, the DNN model enables simulating the competition of tens of thousands of needles, while a corresponding phase-field simulation on a similar hardware (*i.e.* one GPU) would likely be limited to one primary branch with a handful of secondary branches. This computational advantage of the DNN approach stems from the fact that the spatial grid spacing can be chosen of the same order as the steady dendrite tip radius, *i.e.*, one order of magnitude coarser than that required for quantitative phase-field simulation, hence yielding simulations four to five orders of magnitude faster.[74,75] Since the final measured eutectic fraction remains close to a simple Gulliver-Scheil approximation (see Section III–B), one easy approximate solution to overcome DNN limitations to simulate late-stage solidification would be to produce a virtual microstructure by adjusting the width of the predicted dendritic skeleton to match the given final dendritic/eutectic volume fraction. However, while this approach might provide a useful way to overcome this DNN limitation, we chose here to solely use the data from microtomography as input of the micromechanical simulations. Further limitations of the model in reproducing the present experimental observations relate to the fact that we are only simulating a single grain, and that mechanical stresses in the solid structure, which could yield to dendritic fragmentation as in Figure 4(d), are not accounted for. The former limitation can be easily tackled using a numerical implementation with rotated grains (as in, *e.g.*, References 95 and 96). The latter is more challenging as it involves the inclusion of additional physics into the model. A first implementation accounting for fluid dynamics in the liquid phase is currently in progress.

B. *Microstructure*

In the micro-CT tomograms (Figure 6), the eutectic appears as a single, highly attenuating quasi-homogeneous "phase," since the individual lamellae are not resolved. The individual thickness of the lamellae in the eutectic, typically below a micrometer, is smaller than the resolution of micro-CT images of the entire tensile specimen gauge sections. Therefore, the distinct lamellae of the eutectic, although possessing X-ray attenuation contrast with one another, were not resolved and together appeared as a single "phase" that is rich in relatively highly attenuating Cu.

On the other hand, the spatial resolution of the micro-CT tomograms was sufficient to describe the overall geometry of the tensile specimens and gave an accurate representation of the Al-rich dendrite structures, with individual arms clearly distinguished from one another. The most notable segmentation inaccuracies appear in the narrowest channels between the secondary dendrite arms. In such regions, illustrated with the two zoomed-in areas in Figures 7(a) and (b), some eutectic between adjacent secondary arms appear to have been filtered out compared to the grayscale image.

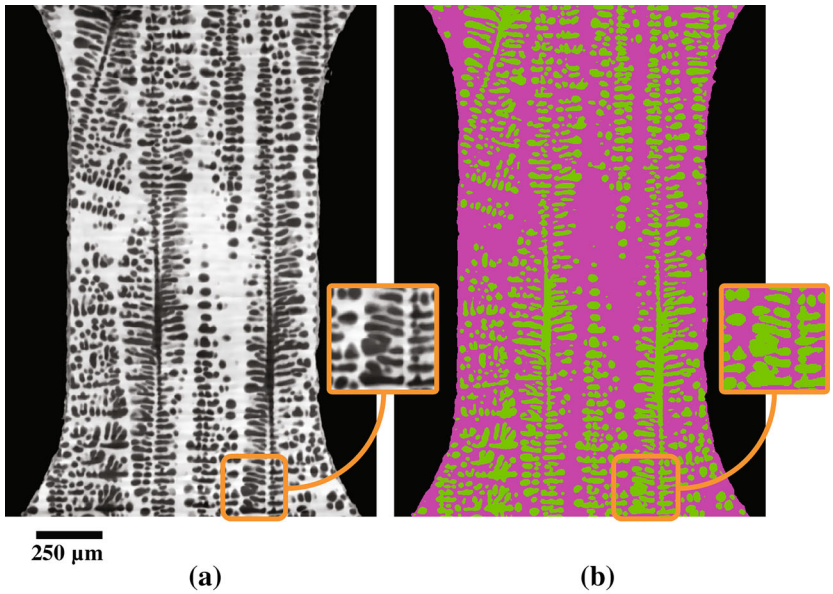

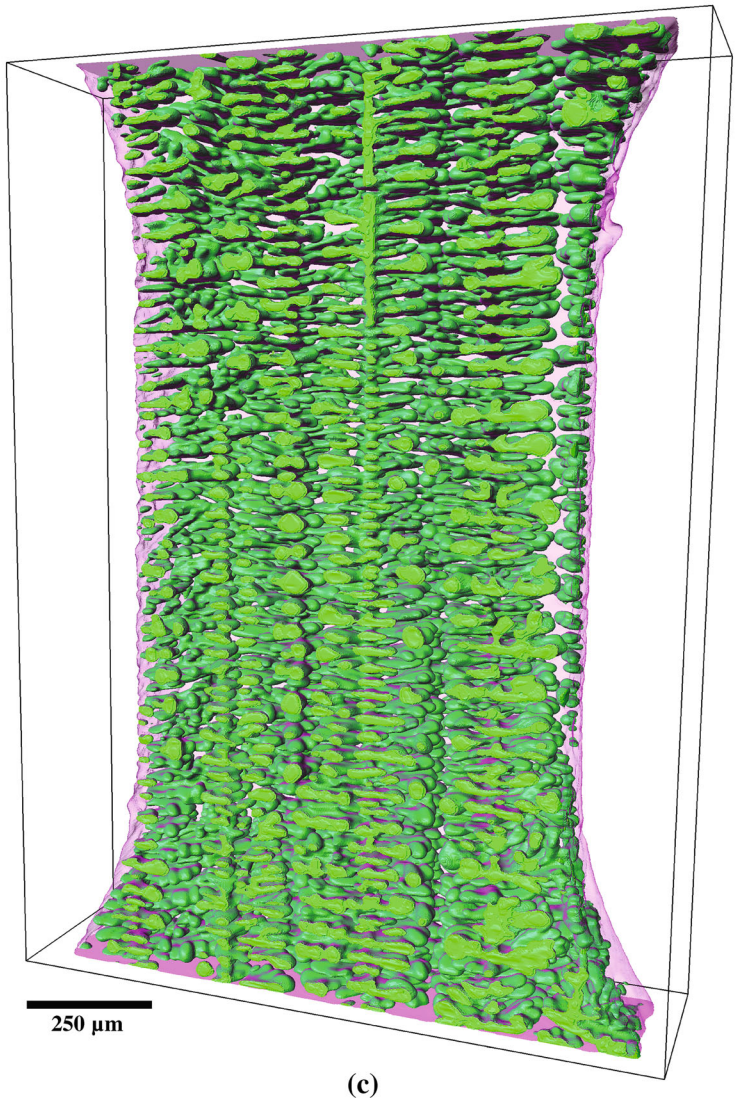

Fig. 7—A single slice of the tomogram, (*a*) before and (*b*) after segmentation into air (black), Al-rich dendrites (green), and ($Al + Al_2Cu$) eutectic (magenta), and (*c*) 3D rendering of the segmented sample, used as input of micromechanical simulations (Color figure online).

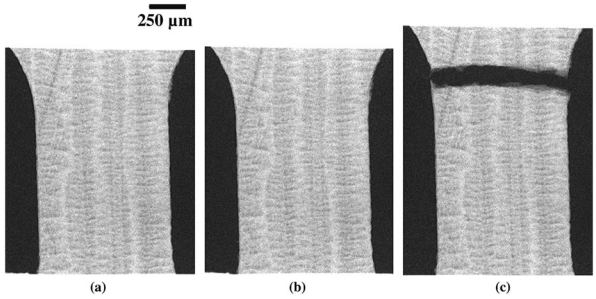

Fig. 8—X-ray radiographs acquired during tensile loading at times t = (*a*) 12, (*b*) 20, and (*c*) 21 s.

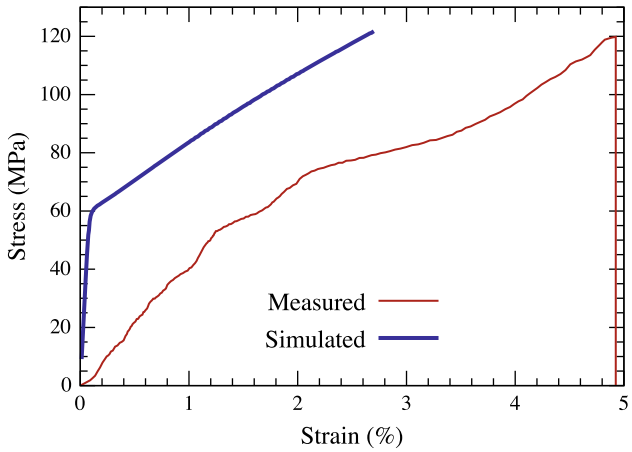

Fig. 9—Measured tensile stress–strain during tensile testing (thin red line), with stress variation derived from cross-sectional area variation, and simulated (thick blue line) after fitting the hardening parameters to the yield stress and failure stress. Errors in the strain measurement, discussed in Section IV–C, are primarily responsible for differences between the experimental and simulated curves.

C. *Mechanical Properties*

The load values from tensile testing were based on the configuration of the tension apparatus, and the measured cross-sectional areas were measured precisely from micro-CT tomograms. Therefore, the calculated engineering stress values should be accurate. On the other hand, we suspect displacement results to have been affected by fixture displacements, some amount of clamping slippage, and to a minor extent machine compliance. Therefore, values of σ_Y and σ_{UTS} are believed to be representative of the sample behavior, whereas E and ε_f, which rely on displacement values, might lack accuracy.

Tensile testing of such miniaturized samples proved to be a challenging task on several aspects. The surface roughness effects, particularly in the filet regions, are believed to have an enhanced effect. Laser machining, used to fabricate the tensile specimens in order to avoid any mechanical damage, results in rougher surface than desirable, as can be seen in Figure 6. The testing fixture used for this study is ideally suited for samples of larger gauge lengths based on the motor travel and load frame geometry. On the one hand, over-tightening of the grip section clamps could potentially damage the tensile samples. On the other hand, under-tightening can cause erroneous displacement values, due to potential slippage of the sample in the clamp. The latter effect could be circumvented by mounting an extensometer to the gauge section itself, but this could prove extremely challenging due to the miniaturized setup.

Due to uncertainty sources mentioned above, *i.e.*, fixture displacements, clamping slippage, and machine compliance, we concluded that the displacement readout from the loading fixture is not to be relied upon. Measurement errors may have come from the load frame itself, thus explaining the unusual shape of the calculated stress–strain curve, specifically a plateau near the center of the curve. This is supported by the observation of relatively little displacement between the grips prior to sample failure, although a large displacement was recorded. During tensile testing, the pins in sample grip section were in place before tightening the sample grips; if not fully engaged prior to testing, grip slippage could also have contributed to a displacement overestimation. Measurement of far-field displacement throughout tensile testing by imaging means would have been a better approach. Unfortunately for this experiment, the frame rate was not sufficient.

Displacement overestimation explains why the elastic constant was estimated at roughly 4 GPa, in sharp contrast with usual values of 70 GPa for Al and 100 GPa for Al_2Cu. The underestimation of the elastic modulus in the experiment appears clearly when compared to simulated results in Figure 9. However, while the slope of the experimental and numerical stress–strain curves differ significantly in the elastic regime, they show a reasonable agreement in the plastic regime. It is worth noting that, as mentioned in Section III–C–3, the yield stress and failure stress are the only two measurements used to calibrate simulation parameters (namely the Voce hardening parameters). Other parameters were identified as detailed in Section II–C–3. (On the other hand, parameters in the DNN simulation only include material parameters from the literature, including previous studies on the Al-Cu system *e.g.* Reference 11, together with measured control parameters, namely temperature gradient and cooling rate, used as input of the simulation.)

Statistical values in Table I show that the region labeled I in Figure 11(b) experienced on average larger stresses, strains, and elastic and plastic work than the other regions. In Figure 12, we plot the (a) normal and (b) shear components of traction along the dendritic–eutectic interface within these four regions. Regions I and II show a slightly higher distribution of high normal traction component around 110 MPa (circled in Figure 12(a)). Region I also shows a significantly higher distribution of shear traction component around 55 to 60 MPa (circled in Figure 12(b)). These results show that regions I and II contain more highly stressed dendritic–eutectic interfaces than the others, thus indicating that the half of the sample containing these regions is the most likely to undergo damage and failure

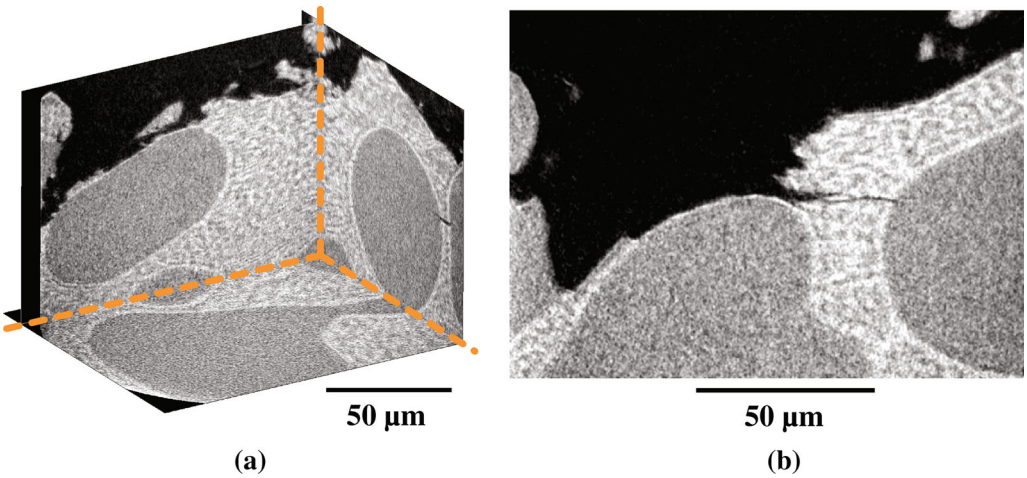

Fig. 10—Nano-CT tomogram of a subset of a fracture surface after tensile failure in the Al-12 at. pct Cu tensile specimen, showing (*a*) orthogonal cross-sections, and (*b*) a single cross-section.

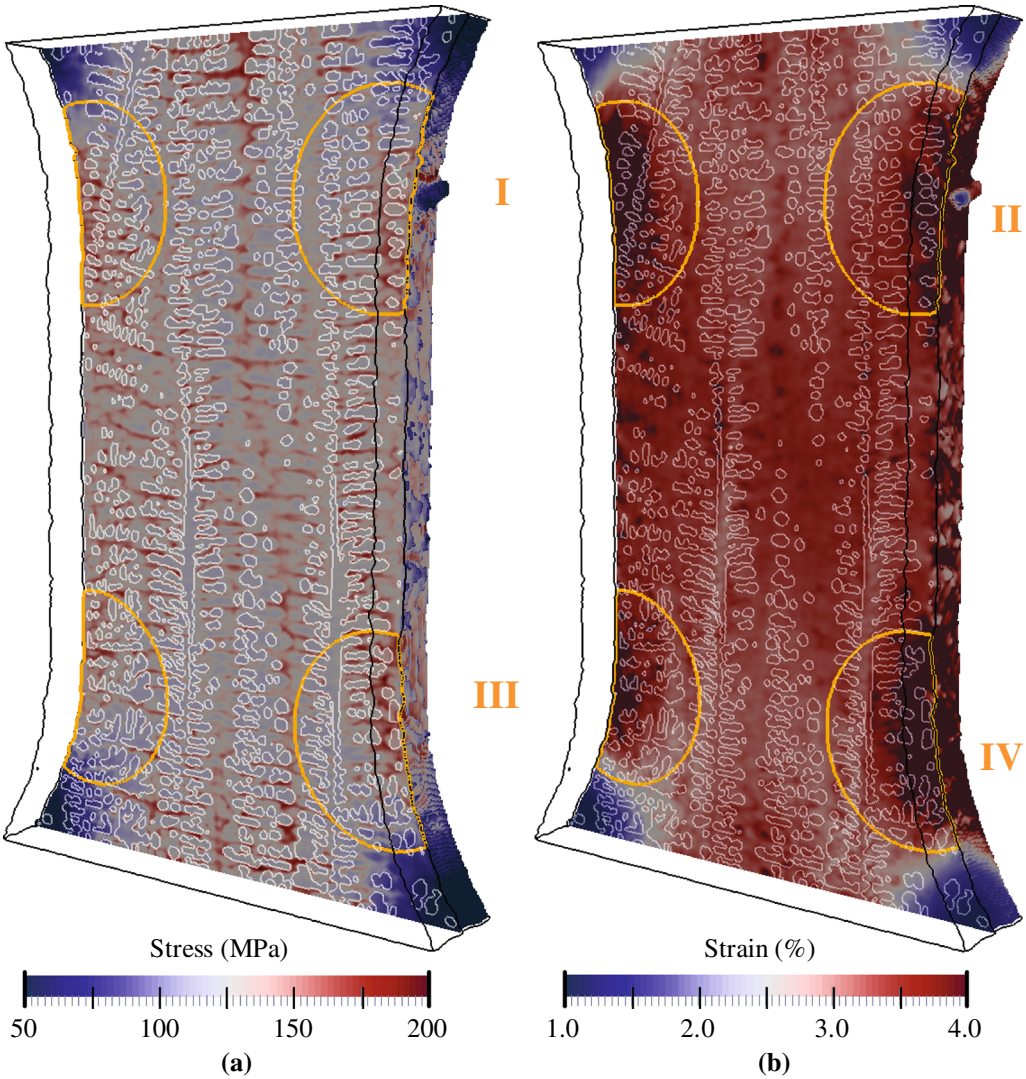

Fig. 11—Simulated von Mises equivalent (*a*) stress and (*b*) strain in the microstructure. Only half of the simulation domain is shown to illustrate the stress and strain states through the center plane of the sample. Edges of the entire solid domain appear in black, and intersections of the dendritic–eutectic interface with the center plane in semi-transparent white lines. Orange circles show the location of the localized measurements in regions of largest curvature in the sample geometry.

Table I. Local Volume Averaged Values of von Mises Equivalent Stress, Hydrostatic Stress, von Mises Equivalent Strain, Elastic Strain Energy, and Plastic Strain Energy for Each Region I Through IV Marked on Fig. 11(b), with the Highest Value Among the Four Regions in Bold Font

	σ_{vm} (MPa)	σ_{hyd} (MPa)	ε_{vm}	Elastic Strain Energy (J/m^3)	Plastic Strain Energy (J/m^3)
Region I	**127.72**	**44.68**	**0.0377**	**0.121**	**2.710**
Region II	124.58	43.65	0.0352	0.114	2.498
Region III	121.73	42.14	0.0344	0.110	2.380
Region IV	125.58	44.01	0.0365	0.118	2.599

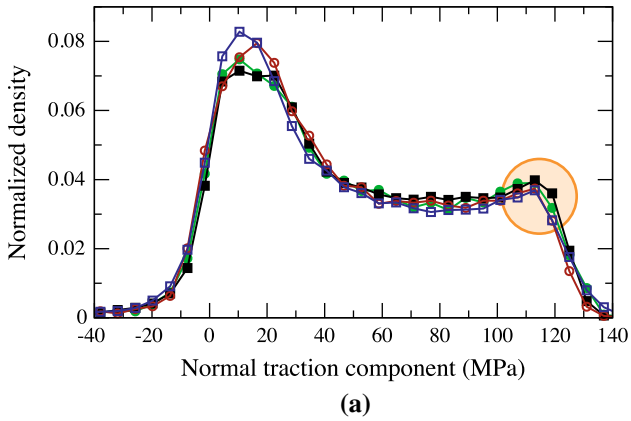

Fig. 12—Distribution of (*a*) normal and (*b*) shear component of traction along the dendritic–eutectic interface within the regions of largest sample curvature (see Fig. 11(b)). Circled regions in (a) and (b), discussed in the text, show that regions I and II contain more highly stressed dendritic–eutectic interfaces.

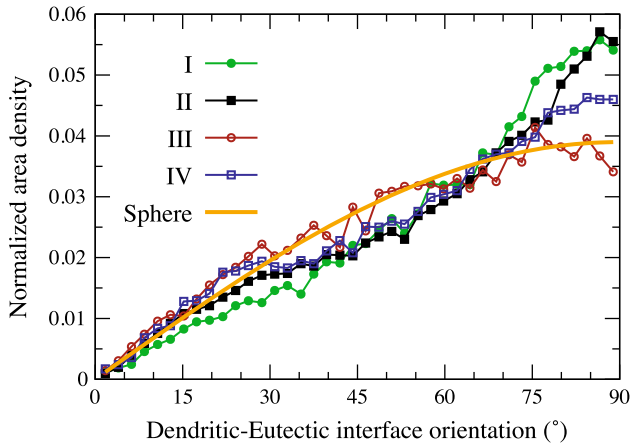

Fig. 13—Angle distributions between the dendritic–eutectic normal angle and the tensile direction within the regions of largest sample curvature (see Fig. 11(b)), compared to the expected distribution for a sphere.

(phenomena not explicitly modeled with the adopted EVPFFT approach), which is consistent with the outcome of the tensile experiment.

The normal and shear traction components of Figure 12 can be directly related to the 3D morphology of the microstructure and the distribution of dendritic–eutectic interface orientation. In Figure 13, we plot the distributions of angle between the orientation of the dendritic–eutectic interface and the loading direction, obtained directly from the discrete voxelized microstructure, using a technique described elsewhere.[97] (These surface normals actually enter the calculation of the normal and shear traction component of Figure 12, obtained by projecting the stress tensor onto the surface normal vector and splitting the resulting vector into a normal and a shear component of traction.) Figure 13 shows that the dendritic–eutectic interface orientation distributions in regions III and IV remain fairly close to the distribution expected for a sphere (thick orange line). On the other hand, regions I and II have higher concentrations of dendritic–eutectic interfaces with an inclination close to 90 deg from the loading direction, making them more likely to experience damage and ultimately failure. Moreover, the fact that region I contains one primary dendrite branch that is slightly more tilted with respect to the loading condition (see Figures 6 and 7), combined with larger deformation and interfacial shear stress, are indicators that failure most likely originated in this region.

D. *Fracture Analysis*

Following the fracture surface from left to right in Figure 10(b), the fracture path is first seen through the Al-rich dendrite. Then, the crack appears to have intercepted a dendrite–eutectic interface, and followed along the interface before jumping across the thin eutectic layer to travel along another dendrite–eutectic interface. The crack path along these dendrite eutectic interfaces seems to remain between the eutectic structure and a thin Al_2Cu "skin" layer immediately surrounding the dendrite. Next, the fracture exhibits a branching event: the top branch propagates through the eutectic to travel along another dendrite–eutectic interface, while the lower branch propagates through the eutectic before

being arrested by a dendrite of the relatively ductile Al dendrite. The overall path of the fracture throughout the entire sample is tortuous, but it distinctly appears to preferably advance along the eutectic–dendrite interfaces, occasionally propagating through either the dendrite or the eutectic, similarly as in the subset illustrated in Figure 10.

V. SUMMARY AND OUTLOOK

In this paper, we have attempted to follow a single Al-Cu alloy sample from its liquid state up to its mechanical failure. We have used *in situ* X-ray radiography to image directional solidification processing (synchrotron X-ray) and tensile testing of the as-solidified sample (microfocus X-ray), as well as microfocus X-ray micro- and nanotomography to image the sample before and after mechanical testing, respectively.

Both processing and mechanical testing steps were directly compared to predictive simulations performed at the length and time scales of the experiments. Namely, we used a multi-scale dendritic needle network (DNN) approach for dendritic solidification, and an elasto-viscoplastic fast Fourier transform (EVPFFT) approach accounting for a voxelized description of the microstructure to simulate tensile testing. These approaches are capable of establishing quantitative links between processing, microstructure, and properties. The DNN simulation provides a good prediction of microstructural lengths resulting from alloy and processing parameters, *e.g.* dendritic spacings. The EVPFFT simulation can predict stress and strain distributions within the sample, and thus identify which regions of the microstructure are more prone to be at the origin of mechanical failure.

The most significant conclusions of the current exploratory study reside in the identification of some major limitations remaining on the way to a complete through-process *in situ* imaging approach, fully coupled with virtual processing and testing tools.

In terms of simulations, while the DNN model is to date the only method capable of quantitatively simulating tens of thousands of dendritic branches at experimentally relevant length and time scales, it is limited to early-stage solidification. It is therefore not capable of generating fully solid microstructures ready-to-use in a micromechanical simulation (or in an intermediate solid-state processing step simulation). In its current early state of development, the method also does not account for mechanical stresses within the dendritic network, which can have significant implication such as dendritic fragmentation. The minor limitation pertaining to the current single-crystal implementation can easily be overcome with an implementation accounting for crystal randomly oriented with respect to the numerical grid (see *e.g.,* References 95 and 96).

Additionally, we have adopted an indirect coupling strategy, modeling the processing and the mechanical testing steps separately. Some major solidification defects, such as hot tears in casting, are intrinsically linked to the coupling between fluid and solid mechanics with solidification dynamics. Development of further multi-physics and multi-scale coupling strategies, an increasingly active area of research, are required to advance the understanding of such complex phenomena.

In terms of experiments, the miniaturizing of standard tensile testing comes with challenges, for instance pertaining to the appropriate clamping of the sample, machine compliance, or to the precise measurement of small deformations. These challenges are already well acknowledged in the growing field of micro- and nanomechanical testing, which has been very active for over a decade (see *e.g.,* References 98 through 101). In this study, some issues related to tensile test miniaturization could, to some extent, be tackled by increasing the size of the sample, for instance benefiting from recent advances in fast 3D tomography (*e.g.*, References 28 and 29). However, increasing the size of the sample would also lead to higher levels of liquid buoyancy during solidification, potentially yielding inhomogeneous microstructures and additional defects.[11,76–78]

In terms of X-ray imaging, main limitations pertain to spatial and temporal resolution versus size of the sample. In the current study, in order to image the entire tensile sample, the resolution from a microfocus tomography scan (Figure 6) was not sufficient to resolve the sub-micron eutectic two-phase structure, and led to some segmentation artifacts (Figure 7). Moreover, using the current microfocus radiography setup, the temporal resolution was not sufficient to make any observation of deformation prior to the onset of the crack, nor that of its propagation within the sample (Figure 8). The trade-off between size of the imaged domain and spatiotemporal accuracy is a well known issue. Those limitations are pushed further every day with the development of increasingly intense and coherent synchrotron X-ray sources, as well as microfocus lab-scale sources, and that of fast imaging techniques (see *e.g.*, Reference 38).

In conclusion, a complete understanding of key mechanisms in the life cycle of structural materials, as well as the development of fully coupled virtual processing and virtual testing tools, remain long-term objectives, but they seem to be within sight. To sustain progress in this general direction, efforts are necessary in the fields of *in situ* imaging, micro- and nanomechanical testing, and predictive multi-physics and multi-scale modeling. Further collaborative studies combining all three aspects should help identifying major hurdles remaining along the way.

ACKNOWLEDGMENTS

This study was supported by the U.S. Department of Energy through the LANL/LDRD Program and by AJC's Early Career award from the U.S. DOE, Office of Basic Energy Sciences, Division of Materials Sciences, Award No. DE-SC0016061. DT gratefully acknowledges support by a Director's Postdoctoral Fellowship from the U.S. Department of Energy through the LANL/LDRD Program. Los Alamos National Laboratory is operated by Los Alamos National

Security LLC under contract number DE-AC52-06-NA25396 for the U.S. Department of Energy. This research used resources of the Advanced Photon Source, a U.S. Department of Energy (DOE) Office of Science User Facility operated for the DOE Office of Science by Argonne National Laboratory under Contract No. DE-AC02-06CH11357.

OPEN ACCESS

REFERENCES

1. R. Stock: *Int. Mater. Rev.*, 2008, vol. 53, pp. 129–81.
2. L. Salvo, M. Suéry, A. Marmottant, N. Limodin, and D. Bernard: *C. R. Phys.*, 2010, vol. 11, pp. 641–49.
3. H. Nguyen-Thi, L. Salvo, R.H. Mathiesen, L. Arnberg, B. Billia, M. Suéry, and G. Reinhart: *C. R. Phys.*, 2012, vol. 13, pp. 237–45.
4. M. Suéry, S. Terzi, B. Mireux, L. Salvo, J. Adrien, and E. Maire: *JOM*, 2012, vol. 64, pp. 83–88.
5. J. Baruchel, M. Di Michiel, T. Lafford, P. Lhuissier, J. Meyssonnier, H. Nguyen-Thi, A. Philip, P. Pernot, L. Salvo, and M. Scheel: *C. R. Phys.*, 2013, vol. 14, pp. 208–20.
6. J.-Y. Buffière, E. Maire, J. Adrien, J.-P. Masse, and E. Boller: *Exp. Mech.*, 2010, vol. 50, pp. 289–305.
7. E. Maire and P.J. Withers: *Int. Mater. Rev.*, 2014, vol. 59, pp. 1–43.
8. R.H. Mathiesen, L. Arnberg, F. Mo, T. Weitkamp, and A. Snigirev: *Phys. Rev. Lett.*, 1999, vol. 83, pp. 5062–65.
9. T. Schenk, H. Nguyen-Thi, J. Gastaldi, G. Reinhart, V. Cristiglio, N. Mangelinck-Noël, H. Klein, J. Härtwig, B. Grushko, B. Billia, and J. Baruchel: *J. Cryst. Growth*, 2005, vol. 275, pp. 201–08.
10. G. Reinhart, N. Mangelinck-Noël, H. Nguyen-Thi, T. Schenk, J. Gastaldi, B. Billia, P. Pino, J. Härtwig, and J. Baruchel: *Mater. Sci. Eng. A*, 2005, vols. 413–414, pp. 384–88.
11. A.J. Clarke, D. Tourret, Y. Song, S.D. Imhoff, P.J. Gibbs, J.W. Gibbs, K. Fezzaa, and A. Karma: *Acta Mater.*, 2017, vol. 129, pp. 203–16.
12. R.H. Mathiesen, L. Arnberg, K. Ramsøskar, T. Weitkamp, C. Rau, and A. Snigirev: *Metall. Mater. Trans. B*, 2002, vol. 33B, pp. 613–23.
13. R.H. Mathiesen and L. Arnberg: *Acta Mater.*, 2005, vol. 53, pp. 947–56.
14. B.M. Patterson, K.C. Henderson, P.J. Gibbs, S.D. Imhoff, and A.J. Clarke: *Mater. Charact.*, 2014, vol. 95, pp. 18–26.
15. A.J. Clarke, D. Tourret, S.D. Imhoff, P.J. Gibbs, K. Fezzaa, J.C. Cooley, W.K. Lee, A. Deriy, B.M. Patterson, P.A. Papin, K.D. Clarke, R.D. Field, and J.L. Smith: *Adv. Eng. Mater.*, 2015, vol. 17, pp. 454–59.
16. R.H. Mathiesen, L. Arnberg, P. Bleuet, and A. Somogyi: *Metall. Mater. Trans. A*, 2006, vol. 37A, pp. 2515–24.
17. D. Ruvalcaba, R.H. Mathiesen, D.G. Eskin, L. Arnberg, and L. Katgerman: *Acta Mater.*, 2007, vol. 55, pp. 4287–92.
18. H. Yasuda, I. Ohnaka, K. Kawasaki, A. Sugiyama, T. Ohmichi, J. Iwane, and K. Umetani: *J. Cryst. Growth*, 2004, vol. 262, pp. 645–52.
19. G. Reinhart, A. Buffet, H. Nguyen-Thi, B. Billia, H. Jung, N. Mangelinck-Noël, N. Bergeon, T. Schenk, J. Härtwig, and J. Baruchel: *Metall. Mater. Trans. A*, 2008, vol. 39A, pp. 865–74.
20. J.W. Gibbs, D. Tourret, P.J. Gibbs, S.D. Imhoff, M.J. Gibbs, B.A. Walker, K. Fezzaa, and A.J. Clarke: *JOM*, 2016, vol. 68, pp. 170–77.
21. S. Karagadde, L. Yuan, N. Shevchenko, S. Eckert, and P.D. Lee: *Acta Mater.*, 2014, vol. 79, pp. 168–80.
22. A. Saad, Ch.-A. Gandin, M. Bellet, N. Shevchenko, and S. Eckert: *Metall. Mater. Trans. A*, 2014, vol. 46A, pp. 4886–97.
23. O. Ludwig, M. Di Michiel, L. Salvo, M. Suéry, and P. Falus: *Metall. Mater. Trans. A*, 2005, vol. 36A, pp. 1515–23.
24. N. Limodin, L. Salvo, M. Suéry, and M. Di Michiel: *Acta Mater.*, 2007, vol. 55, pp. 3177–91.
25. N. Limodin, L. Salvo, E. Boller, M. Suéry, M. Felberbaum, S. Gaillièque, and K. Madi: *Acta Mater.*, 2009, vol. 57, pp. 2300–10.
26. C. Puncreobutr, A.B. Phillion, J.L. Fife, P. Rockett, A.P. Horsfield, and P.D. Lee: *Acta Mater.*, 2014, vol. 79, pp. 292–303.
27. C. Puncreobutr, A.B. Phillion, J.L. Fife, and P.D. Lee: *Acta Mater.*, 2014, vol. 64, pp. 316–25.
28. J.W. Gibbs, K.A. Mohan, E.B. Gulsoy, A.J. Shahani, X. Xiao, C.A. Bouman, M. De Graef, and P.W. Voorhees: *Sci. Rep.*, 2015, vol. 5, p. 11824.
29. S. Shuai, E. Guo, A.B. Phillion, M.D. Callaghan, T. Jing, and P.D. Lee: *Acta Mater.*, 2016, vol. 118, pp. 260–69.
30. B. Cai, J. Wang, A. Kao, K. Pericleous, A.B. Phillion, R.C. Atwood, and P.D. Lee: *Acta Mater.*, 2016, vol. 117, pp. 160–69.
31. R. Daudin, S. Terzi, P. Lhuissier, J. Tamayo, M. Scheel, N. Hari Babu, D.G. Eskin, and L. Salvo: *Acta Mater.*, 2017, vol. 125, pp. 303–10.
32. S. Youssef, E. Maire, and R. Gaertner: *Acta Mater.*, 2005, vol. 53, pp. 719–30.
33. J. Rannou, N. Limodin, J. Réthoré, A. Gravouil, W. Ludwig, M.-C. Baïetto-Dubourg, J.-Y. Buffière, A. Combescure, F. Hild, and S. Roux: *Comput. Meth. Appl. Mech. Eng.*, 2010, vol. 199, pp. 1307–25.
34. E. Maire, S. Zhou, J. Adrien, and M. Di Michiel: *Eng. Fract. Mech.*, 2011, vol. 78, pp. 2679–90.
35. S. Thuillier, E. Maire, and M. Brunet: *Mater. Sci. Eng. A*, 2012, vol. 558, pp. 217–25.
36. T. Zhang, E. Maire, J. Adrien, P.R. Onck, and L. Salvo: *Adv. Eng. Mater.*, 2013, vol. 15, pp. 767–72.
37. C. Betts, D. Balint, J. Lee, J. Lin, and P. Lee: *J. Strain Anal. Eng.*, 2014, vol. 49, pp. 592–606.
38. E. Maire, C. Le Bourlot, J. Adrien, A. Mortensen, and R. Mokso: *Int. J. Fract.*, 2016, vol. 200, pp. 3–12.
39. A.B. Phillion, P.D. Lee, E. Maire, and S.L. Cockroft: *Metall. Mater. Trans. A*, 2008, vol. 39A, pp. 2459–69.
40. S. Terzi, L. Salvo, M. Suéry, N. Limodin, J. Adrien, E. Maire, Y. Pannier, M. Bornert, D. Bernard, M. Felberbaum, M. Rappaz, and E. Boller: *Scr. Mater.*, 2009, vol. 61, pp. 449–52.
41. J.-F. Zaragoci, L. Silva, M. Bellet, and Ch.-A. Gandin: *IOP Conf. Ser. Mater. Sci. Eng.*, 2012, vol. 33, p. 012054.
42. J.-F. Zaragoci: *Simulation numérique directe multiphasique de la déformation d'un alliage Al-Cu à l'état pâteux - Comparaison avec des observations par tomographie aux rayons X in situ en temps réel*, Ph.D. Thesis, Ecole Nationale Supérieure des Mines de Paris, 2012.
43. C. Puncreobutr, P.D. Lee, R.W. Hamilton, B. Cai, and T. Connoley: *Metall. Mater. Trans. A*, 2013, vol. 44A, pp. 5389–95.
44. M. Sistaninia, S. Terzi, A.B. Phillion, J.-M. Drezet, and M. Rappaz: *Acta Mater.*, 2013, vol. 61, pp. 3831–41.
45. B. Cai, S. Karagadde, L. Yuan, T.J. Marrow, T. Connolley, and P.D. Lee: *Acta Mater.*, 2014, vol. 76, pp. 371–80.
46. K.M. Kareh, P.D. Lee, R.C. Atwood, T. Connolley, and C.M. Gourlay: *Nat. Commun.*, 2014, vol. 5, p. 4464.
47. S. Karagadde, P.D. Lee, B. Cai, J.L. Fife, M.A. Azeem, K.M. Kareh, C. Puncreobutr, D. Tsivoulas, T. Connolley, and R.C. Atwood: *Nat. Commun.*, 2015, vol. 6, p. 8300.
48. B. Cai, P.D. Lee, S. Karagadde, T.J. Marrow, and T. Connolley: *Acta Mater.*, 2016, vol. 105, pp. 338–46.
49. H.F. Poulsen: *Three-Dimensional X-ray Diffraction Microscopy: Mapping Polycrystals and Their Dynamics*, Springer, New York, 2004.
50. U. Lienert, S.F. Li, C.M. Hefferan, J. Lind, R.M. Suter, J.V. Bernier, N.R. Barton, M.C. Brandes, M.J. Mills, M.P. Miller, and B. Jakobsen: *JOM*, 2011, vol. 63, pp. 70–77.
51. R.M. Suter, D. Hennessy, C. Xiao, and U. Lienert: *Rev. Sci. Instrum.*, 2006, vol. 77, p. 123905.
52. G. Johnson, A. King, M. Goncalves Honnicke, J. Marrow, and W. Ludwig: *J. Appl. Crystallogr.*, 2008, vol. 41, pp. 310–18.

53. J. Oddershede, S. Schmidt, H.F. Poulsen, L. Margulies, J. Wright, M. Moscicki, W. Reimers, and G. Winther: *Mater. Charact.*, 2011, vol. 62, pp. 651–60.
54. J.V. Bernier, N.R. Barton, U. Lienert, and M.P. Miller: *J. Strain Anal. Eng.*, 2011, vol. 46, pp. 527–47.
55. M. Asta, C. Beckermann, A. Karma, W. Kurz, R. Napolitano, M. Plapp, G. Purdy, M. Rappaz, and R. Trivedi: *Acta Mater.*, 2009, vol. 57, pp. 941–71.
56. A. Karma and D. Tourret: *Curr. Opin. Solid State Mater. Sci.*, 2016, vol. 20, pp. 25–36.
57. M. Rappaz: *Curr. Opin. Solid St. Mater. Sci.*, 2016, vol. 20, pp. 37–45.
58. J.W. Hutchinson: *Proc. R. Soc. Lond. A*, 1976, vol. 348, pp. 101–27.
59. R.A. Lebensohn and C.N. Tomé: *Acta Metall. Mater.*, 1993, vol. 41, pp. 2611–24.
60. P. Ponte Castañeda and P. Suquet: *Adv. Appl. Mech.*, 1998, vol. 34, pp. 171–302.
61. H. Moulinec and P. Suquet: *Comput. Meth. Appl. Mech. Eng.*, 1998, vol. 157, pp. 69–94.
62. R.A. Lebensohn: *Acta Mater.*, 2001, vol. 49, pp. 2723–37.
63. N. Moës, M. Cloirec, P. Cartraud, and J.-F. Remacle: *Comput. Meth. Appl. Mech. Eng.*, 2003, vol. 192, pp. 3163–77.
64. G. Cailletaud, S. Forest, D. Jeulin, F. Feyel, I. Galliet, V. Mounoury, and S. Quilici: *Comput. Mater. Sci.*, 2003, vol. 27, pp. 351–74.
65. R.A. Lebensohn, A.K. Kanjarla, and P. Eisenlohr: *Int. J. Plast.*, 2012, vols. 32–33, pp. 59–69.
66. R. Pokharel, J. Lind, A.K. Kanjarla, R.A. Lebensohn, S.F. Li, P. Kenesei, R.M. Suter, and A.D. Rollett: *Annu. Rev. Condens. Matter Phys.*, 2014, vol. 5, pp. 317–46.
67. R. Pokharel, J. Lind, S.F. Li, P. Kenesei, R.A. Lebensohn, R.M. Suter, and A.D. Rollett: *Int. J. Plast.*, 2015, vol. 67, pp. 217–34.
68. E. Lieberman, R.A. Lebensohn, D.B. Menasche, C.A. Bronkhorst, and A.D. Rollett: *Acta Mater.*, 2016, vol. 116, pp. 270–80.
69. R. Pokharel and R.A. Lebensohn: *Scr. Mater.*, 2017, vol. 132, pp. 73–77.
70. P. Ackermann and W. Kurz: *Mater. Sci. Eng.*, 1985, vol. 75, pp. 79–85.
71. T.B. Kim, S. Yue, Z. Zhang, E. Jones, J.R. Jones, and P.D. Lee: *J. Mater. Process. Tech.*, 2014, vol. 214, pp. 2706–15.
72. T. Koshikawa, M. Bellet, Ch.-A. Gandin, H. Yamamura, and M. Bobadilla: *Metall. Mater. Trans. A*, 2016, vol. 47A, pp. 4053–67.
73. T. Koshikawa, M. Bellet, Ch.-A. Gandin, H. Yamamura, and M. Bobadilla: *Acta Mater.*, 2017, vol. 124, pp. 513–27.
74. D. Tourret and A. Karma: *Acta Mater.*, 2013, vol. 61, pp. 6474–91.
75. D. Tourret and A. Karma: *Acta Mater.*, 2016, vol. 120, pp. 240–54.
76. A. Bogno, G. Reinhart, A. Buffet, H. Nguyen-Thi, B. Billia, T. Schenk, N. Mangelinck-Noël, N. Bergeon, and J. Baruchel: *J. Cryst. Growth*, 2011, vol. 318, pp. 1134–38.
77. A. Bogno, H. Nguyen-Thi, A. Buffet, G. Reinhart, B. Billia, N. Mangelinck-Noël, N. Bergeon, J. Baruchel, and T. Schenk: *Acta Mater.*, 2011, vol. 59, pp. 4356–65.
78. H. Nguyen-Thi, A. Bogno, G. Reinhart, B. Billia, R.H. Mathiesen, G. Zimmermann, Y. Houltz, K. Löth, D. Voss, and A. Verga: *J. Phys.*, 2011, vol. 327, p. 012012.
79. D. Tourret, A. Karma, A.J. Clarke, P.J. Gibbs, and S.D. Imhoff: *IOP Conf. Ser. Mater. Sci. Eng.*, 2015, vol. 84, p. 012082.
80. D. Tourret, A.J. Clarke, S.D. Imhoff, P.J. Gibbs, J.W. Gibbs, and A. Karma: *JOM*, 2015, vol. 67, pp. 1776–85.
81. A. Barbieri and J.S. Langer: *Phys. Rev. A*, 1989, vol. 39, p. 5314.
82. J.L. Murray: *Int. Metals Rev.*, 1985, vol. 30, pp. 211–33.
83. W. Kurz and D.J. Fisher: *Fundamentals of Solidification*, 3rd ed., Trans Tech Publications, Stafa-Zurich, 1992.
84. M.P. Watson and J.D. Hunt: *Metall. Mater. Trans. A*, 1977, vol. 8A, pp. 1793–98.
85. N. Marasli and J.D. Hunt: *Acta Mater.*, 1996, vol. 44, pp. 1085–96.
86. J.R. Morris: *Phys. Rev. B*, 2002, vol. 66, p. 144104.
87. L. Chen, J. Chen, R.A. Lebensohn, Y.Z. Ji, T.W. Heo, S. Bhattacharyya, K. Chang, S. Mathaudhu, Z.K. Liu, and L.Q. Chen: *Comput. Meth. Appl. Mech. Eng.*, 2015, vol. 285, pp. 829–48.
88. G. Simmons and H. Wang: *Single Crystal Elastic Constants and Calculated Aggregate Properties*, MIT Press, Cambridge, 1971.
89. B. Cantor and G.A. Chadwick: *J. Cryst. Growth*, 1974, vol. 23, pp. 12–20.
90. U. Hecht, V. Witusiewicz, and A. Drevermann: *IOP Conf. Ser. Mat. Sci. Eng.*, 2011, vol. 27, p. 012029.
91. R. Hill: *J. Mech. Phys. Solids*, 1965, vol. 13, pp. 89–101.
92. J. Zhang, Y.N. Huang, C. Mao, and P. Peng: *Solid State Commun.*, 2012, vol. 152, pp. 2100–04.
93. C.S. Tiwary, S. Chakraborty, D.R. Mahapatra, and K. Chattopadhyay: *J. Appl. Phys.*, 2014, vol. 115, p. 203502.
94. R. Lebensohn, H. Uhlenhut, C. Hartig, and H. Mecking: *Acta Mater.*, 1998, vol. 46, pp. 4701–09.
95. P.-A. Geslin, A. Karma: TMS 2016 Annual Meeting, Supplemental Proceedings, Symposium Frontiers in Solidification Science, 2016, pp. 29–34.
96. G. Zimmermann, L. Sturz, H. Nguyen-Thi, N. Mangelinck-Noël, Y.Z. Li, D.-R. Liu, C.-A. Gandin, R. Fleurisson, G. Guillemot, S. McFadden, R.P. Mooney, P. Voorhees, A. Roosz, A. Ronaföldi, C. Beckermann, A. Karma, C.-H. Chen, N. Warnken, A. Saad, G.-U. Grün, M. Grohn, I. Poitrault, T. Pehl, I. Nagy, D. Todt, O. Minster, and W. Sillekens: *JOM*, 2017, vol. 69, pp. 1269–79.
97. E.J. Lieberman, A.D. Rollett, R.A. Lebensohn, and E.M. Kober: *Model. Simul. Mater. Sci.*, 2015, vol. 23, p. 035005.
98. K.J. Hemker and W.N. Sharpe, Jr: *Annu. Rev. Mater. Res.*, 2007, vol. 37, pp. 93–126.
99. D.S. Gianola and C. Eberl: *JOM*, 2009, vol. 61, pp. 24–35.
100. D. Kiener, C. Motz, and G. Dehm: *Mater. Sci. Eng. A*, 2009, vol. 505, pp. 79–87.
101. Y.H. Zhao, Y.Z. Guo, Q. Wei, T.D. Topping, A.M. Dangelewicz, Y.T. Zhu, T.G. Langdon, and E.J. Lavernia: *Mater. Sci. Eng. A*, 2009, vol. 525, pp. 68–77.